Journal of Materials Chemistry A

ROYAL SOCIETY OF CHEMISTRY

PAPER

View Article Online
View Journal | View Issue

Cite this: J. Mater. Chem. A, 2024, 12, 2479

Fluorination promotes lithium salt dissolution in borate esters for lithium metal batteries†

Peiyuan Ma, Ritesh Kumar, Minh Canh Vu, Ke-Hsin Wang, Priyadarshini Mirmira and Chibueze V. Amanchukwu *

Lithium metal batteries promise higher energy densities than current lithium-ion batteries but require novel electrolytes to extend their cycle life. Fluorinated solvents help stabilize the solid electrolyte interphase (SEI) with lithium metal, but are believed to have weaker solvation ability compared to their nonfluorinated counterparts and are deemed 'poorer electrolytes'. In this work, we synthesize tris(2-fluoroethyl) borate (TFEB) as a new fluorinated borate ester solvent and show that TFEB unexpectedly has higher lithium salt solubility than its nonfluorinated counterpart (triethyl borate). Through experiments and simulations, we show that the partially fluorinated $-CH_2F$ group acts as the primary coordination site that promotes lithium salt dissolution. TFEB electrolyte has a higher lithium transference number and better rate capability compared to methoxy polyethyleneglycol borate esters reported in the literature. In addition, TFEB supports compact lithium deposition morphology, high lithium metal Coulombic efficiency, and stable cycling of lithium metal/$LiFePO_4$ cells. This work ushers in a new electrolyte design paradigm where partially fluorinated moieties enable salt dissolution and can serve as primary ion coordination sites for next-generation electrolytes.

Received 13th October 2023
Accepted 11th December 2023

DOI: 10.1039/d3ta06228g

rsc.li/materials-a

Introduction

Lithium metal is viewed as the future of lithium-based batteries because it has an order of magnitude higher specific capacity than commercially used graphitic anodes (in lithium ion batteries).[1] Unfortunately, carbonate-based electrolytes currently used in commercial lithium ion batteries suffer from poor reductive stability and uneven lithium deposition, which result in lithium metal cycling Coulombic efficiencies as low as 50%.[2,3] To promote electrolyte stability against lithium metal and suppress lithium dendrite formation, several electrolyte engineering and electrolyte chemistry approaches have been pursued.[4] For example, high concentration electrolytes (HCEs) and localized high concentration electrolytes (LHCEs) have changed the electrolyte design paradigm.[3,5–8] High or locally high salt concentrations promote the formation of ion pairing and salt aggregates, which can increase the Coulombic efficiency of lithium metal cycling to as high as 99.5%.[9,10] Recently, novel fluoroether solvents have been reported by us and others to support stable lithium metal cycling with Coulombic efficiency as high as 99.9% in single-solvent–single-salt ~1 M electrolytes.[11–14] Other fluorinated cyclic ethers and fluorinated sulfonamides have also been reported to enable efficient lithium metal cycling.[15–20]

Among those novel electrolytes, fluorinated solvents or diluents are frequently used because fluorinated moieties are known to passivate the lithium metal surface with a robust, lithium fluoride rich solid electrolyte interphase (SEI) as well as increase the oxidative stability.[21,22] However, fluorination is also generally believed to weaken solvation ability (or 'solvation strength') of the solvent. For example, fluorinated ether diluents such as bis(2,2,2-trifluoroethyl) ether (BTFE) and tris(2,2,2-trifluoroethyl)orthoformate (TFEO) are known to improve lithium metal cycling but do not dissolve lithium salts while their nonfluorinated counterparts, diethyl ether and triethyl orthoformate, can dissolve lithium salt to concentrations higher than 1 M.[17,23] Although some recently reported fluoroether solvents such as fluorinated glymes,[12,24] fluorinated 1,4-dimethoxybutane (FDMB)[12] and fluorinated 1,2-diethoxyethane (FDEE)[13] can dissolve lithium salt to more than 1 M, the corresponding electrolytes show much lower ionic conductivities compared to their nonfluorinated counterparts (glymes, 1,4-dimethoxybutane and 1,2-diethoxyethane). Hence, there has been an inherent compromise between ionic solvation/conductivity and electrochemical properties such as oxidative stability and SEI passivation. On the other hand, some reports hint that fluorine could potentially act as a coordination site to enhance solvation/conductivity. For example, Rustomji *et al.* reported that monofluorinated alkane gases such as fluoromethane can have ionic conductivity ~1 mS cm^{-1} with 0.1 M

Pritzker School of Molecular Engineering, University of Chicago, IL 60637, USA. E-mail: chibueze@uchicago.edu

† Electronic supplementary information (ESI) available: Additional data and figures including physical data, synthetic scheme, NMR spectra, DFT calculation data, AIMD simulation results, SEM images, EIS data, battery cycling data and DSC data. See DOI: https://doi.org/10.1039/d3ta06228g

LiTFSI salt when liquefied at low temperatures.[25] Recent studies on fluorinated ethers and carbonates also indicate that partially fluorinated groups such as $-CHF_2$ and $-CH_2F$ can coordinate to lithium ions more favorably than perfluoro groups ($-CF_3$ or $-CF_2-$).[14,26] Nonetheless, the coordination ability of fluorinated groups is not well understood and there is still no clear evidence that fluorinated groups alone can enable conventional salt concentrations (~1 M).

Borate ester or boroxine type compounds are well-known Lewis acids. They have been proposed as "anion acceptors" in polymer electrolytes to promote lithium salt dissociation and increase lithium transference number.[27–29] However, rarely are borate esters studied as liquid electrolytes, partly because most commercially available borate esters cannot dissolve enough lithium salt alone. For example, tris(2,2,2-trifluoroethyl) borate has been studied as an additive in electrolytes for lithium metal and lithium-ion batteries but it can barely dissolve lithium salts as a single solvent.[30,31] Kaneko *et al.* studied a group of tris(-methoxy polyethyleneglycol) borate esters as liquid electrolyte solvents.[32] To the best of our knowledge, they are the only group of borate ester solvents that have been reported to dissolve lithium salt up to 1 M. Nonetheless, those nonfluorinated borate esters show very poor cycle life in lithium metal batteries.

Herein, we investigate the influence of fluorination on the ion solvation ability and electrochemical stability of borate esters. We synthesize tris(2-fluoroethyl) borate (TFEB) as a new borate ester solvent. The lithium salt solubility of TFEB is first compared to that of two commercially available compounds: triethyl borate (TEB) and tris(2,2,2-trifluoroethyl) borate (TTFEB). Interestingly, moderately fluorinated TFEB has the highest lithium salt solubility (~1 M) among these three solvents. This indicates that lithium salt dissolution can be promoted by proper fluorination, which challenges the general literature assumption. To explain the unusual salt solubility trend, we investigate the ion solvation environment using density functional theory (DFT) and *ab initio* molecular dynamics (AIMD) simulations. We show that TFEB prefers to bind to lithium through fluorine of the $-CH_2F$ group, which leads to more negative lithium ion binding energy (stronger solvation ability) than TTFEB and TEB. We then study the ion transport and electrochemical properties of 1 M lithium bis-fluorosulfonyl amide (LiFSA) in TFEB as an electrolyte in comparison to the previously reported tris(2-methoxyethyl) borate (TMEB) electrolyte. Despite slightly lower ionic conductivity compared to TMEB, TFEB electrolyte has a higher lithium transference number and can sustain much higher current densities. TFEB electrolyte also produces a denser lithium deposition morphology and higher Coulombic efficiency (97.1% *vs.* 51.7%) than TMEB, which enables stable cycling in lithium metal/$LiFePO_4$ (Li/LFP) full cells.

Results and discussion

Molecular design and synthesis

Borate esters have been widely studied as additives in electrolytes as "anion acceptors", but most borate ester solvents have limited lithium salt solubility.[27–29] As shown in Fig. 1, TEB has three oxygen atoms that could potentially coordinate to the

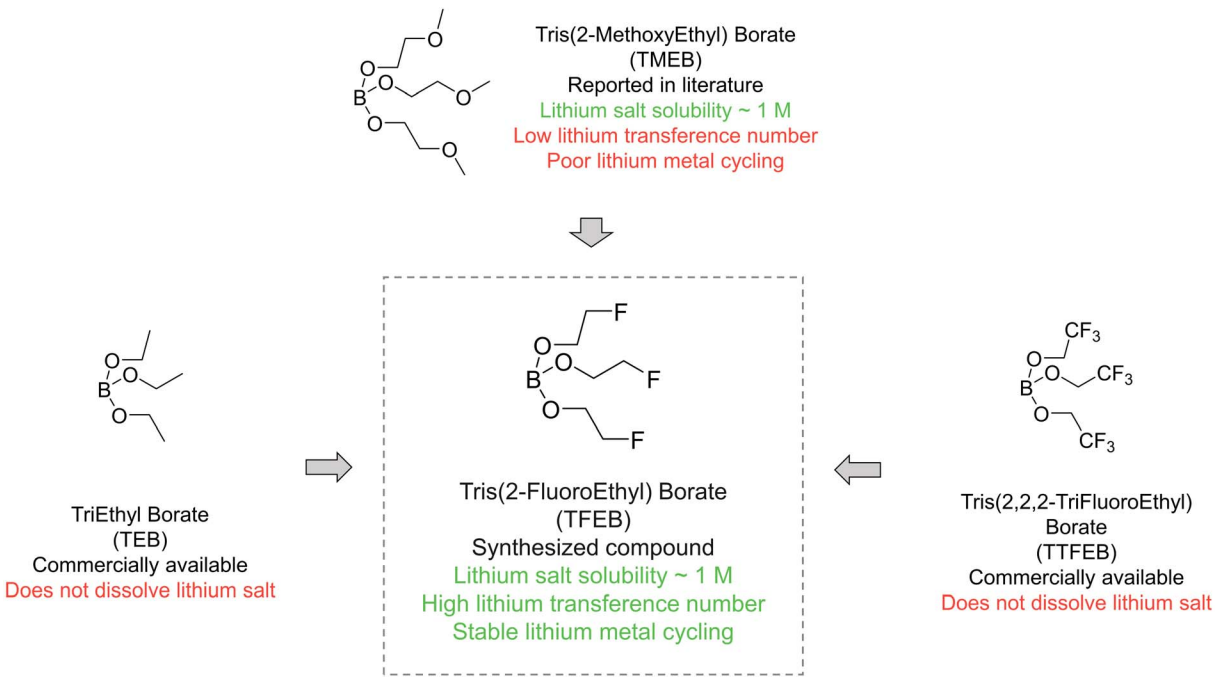

Fig. 1 Molecular design. Most commercially available borate ester solvents such as nonfluorinated triethyl borate (TEB) and heavily fluorinated tris(2,2,2-trifluoroethyl) borate (TTFEB) have limited lithium salt solubility. In this work, we synthesize a new compound, tris(2-fluoroethyl) borate (TFEB), with a tuned fluorination degree. TFEB has higher lithium salt solubility than TEB or TTFEB, making it a relevant electrolyte solvent. Compared to previously reported tris(2-methoxyethyl) borate (TMEB),[32] TFEB electrolyte enables a higher lithium transference number and better stability against lithium metal.

lithium ion but still barely dissolve lithium salt. TTFEB can be viewed as a perfluorinated-methyl-group version of TEB that has been studied as an electrolyte additive to promote lithium metal cycling stability.[30,31] However, TTFEB also has no lithium salt solubility. Tris(methoxy polyethyleneglycol) borate esters such as TMEB, where additional ether units are added as coordination sites, are the only known example that can dissolve lithium salt to concentrations higher than 1 M. Recently, Yu *et al.* illustrated that a partially fluorinated $-CHF_2$ group led to faster ion transport compared to perfluorinated groups.[26] Here, we designed a "partially fluorinated TEB": tris(2-fluoroethyl) borate (TFEB). The structure of TFEB can be viewed as a compromise between TEB and TTFEB. It can also be viewed as analogous to TMEB where the methoxy group is replaced with fluorine. We expect TFEB to maintain the interfacial passivation ability of fluorinated compounds while having a stronger solvating ability compared to TTFEB. TFEB is synthesized through the condensation reaction between boric oxide and 2-fluoroethanol (Fig. S1†). Synthesis and purification procedures were modified from the literature and details can be found in the ESI.†[33] The structure and product purity were verified by ^{1}H, ^{13}C, ^{19}F, and ^{11}B nuclear magnetic resonance (NMR) spectroscopy (Fig. S11†).

Ion solvation structure

The effect of fluorination degree on lithium salt solubility was investigated. Fig. 2a shows digital images of 1 M LiFSA salt (1 mol of salt per 1 liter of solvent) mixed with different borate esters, where TFEB and TMEB can fully dissolve 1 M LiFSA to form a clear solution whereas undissolved salt remains in TEB and TTFEB. To verify salt solubility and study the ion solvation structure, ^{7}Li and ^{19}F NMR was performed on 1 M LiFSA solutions (TFEB and TMEB) or LiFSA saturated solutions (TEB and TTFEB). Fig. 2b shows that no lithium-ion signal is observed in TEB and TTFEB while 1 M LiFSA solutions in TFEB and TMEB have lithium ion signals at −2.36 ppm and −1.97 ppm, respectively. Compared to TMEB, the more upfield ^{7}Li chemical shift in TFEB indicates either more ion pairing or stronger solvent coordination. ^{19}F NMR spectra in Fig. S2† also confirm the poor salt solubilities in TEB and TTFEB as no FSA anion signal is observed. The surprisingly high lithium salt solubility in TFEB compared to TEB and TTFEB indicates that the $-CH_2F$ group likely promotes lithium salt dissolution.

To explain this unexpected lithium salt solubility trend, the interaction energy between lithium ions and borate esters was calculated using density functional theory (DFT). Fig. 2c shows the lithium binding energy with a single solvent molecule, which is defined as $G(\text{solvent} + Li^+) - G(\text{solvent}) - G(Li^+)$. The lithium binding energy trend explains the lithium salt solubility trend as Li^+ binding energy goes less negative from TMEB to TFEB to TEB to TTFEB, which indicates that TFEB has higher salt solubility than TEB and TTFEB because of stronger binding to lithium ions. To probe the differences in ion binding modes, lithium–solvent pair structure optimized in DFT calculations are shown in Fig. S3.† TEB prefers to bind to the lithium ion with the borate ester oxygen since it is the only available binding site. Interestingly, the most favorable lithium binding mode of TFEB is only through the three fluorine atoms and the second most favorable mode binds through two fluorine atoms and one oxygen atom. TTFEB also prefers to bind to the lithium ion with two fluorine atoms and one oxygen atom, but the more positive binding energy indicates that fluorine atoms in $-CF_3$ groups are less available than those in the $-CH_2F$ groups of TFEB. In TMEB, the ether oxygen is preferred for lithium ion coordination over the borate ester oxygen. It is well known that the B–O bond in the borate esters group has a partial sp^2 nature and oxygen lone pairs conjugate to the boron atom,[34] which likely weakens the coordination ability of borate ester oxygens. The binding mode in TFEB suggests that the $-CH_2F$ group can act as a coordination site that is similar to the methoxy group in TMEB.

To further understand the unexpectedly strong solvation ability of TFEB, *ab initio* molecular dynamics (AIMD) simulation was used to simulate the solvation structure of 1 M LiFSA in TFEB. Fig. 2d shows the radial distribution function (RDF) of different binding sites with respect to lithium ions. Consistent with the DFT calculations, the first solvation shell of lithium ions is dominated by oxygen of the FSA anion and fluorine of the TFEB molecule with little contribution from the oxygen of TFEB. The coordination number (N_c) is quantified from the cumulative integration curve as shown in Fig. 2e using 2.5 Å as the cutoff, which also confirms that the lithium ion is mainly coordinated by TFEB fluorine ($N_c = 2.19$) and FSA oxygen ($N_c = 1.77$) instead of TFEB oxygen ($N_c = 0.38$). As an example, Fig. 2f shows a representative solvation environment of lithium ions in TFEB, where the lithium ion is coordinated by two fluorine atoms from TFEB solvent and two oxygen atoms from the FSA anion.

The solvation structure of 1 M LiFSA in TMEB and TFEB electrolytes was also characterized using spectroscopic and electrochemical techniques. Fig. 2g shows Raman spectra corresponding to the FSA stretching and B–O stretching modes. The FSA peak in TFEB has a blue shift to higher wavenumbers compared to TMEB, which indicates that TFEB favors more contact ion pairs (CIP) and salt aggregates (AGG).[35] Assuming a constant solvent background to be subtracted from the FSA peak, the remaining 'true FSA peak' can be fit and a fraction of ion pairing can be roughly quantified. As shown in Fig. 2h, TFEB leads to a much higher fraction of ion pairing (93% AGG and 7% CIP) than TMEB (12% AGG and 36% CIP). Following the protocol recently reported by Ko *et al.*, the lithium redox potential (E_{Li}) in borate ester electrolytes is calibrated to a ferrocene (Fc) internal standard.[36] Fig. 2i shows the cyclic voltammetry curve of borate ester electrolytes containing 1 mM Fc with platinum as the working electrode and lithium metal as the counter and reference electrode. Assuming a constant potential of Fc/Fc^+ as a reference, Li/Li^+ potentials in different electrolytes can be calculated and serve as an indicator of the ion solvation structure. TFEB electrolyte has a E_{Li} of −2.95 V, which is 0.35 V higher than that of TMEB electrolyte (−3.30 V). This indicates that the lithium ion has a weaker binding environment in TFEB and verifies that TFEB leads to an ion solvation structure rich in ion pairing between the cation and anion. As discussed later, the high E_{Li} in TFEB electrolyte leads to more reversible lithium metal cycling as compared to TMEB electrolyte.

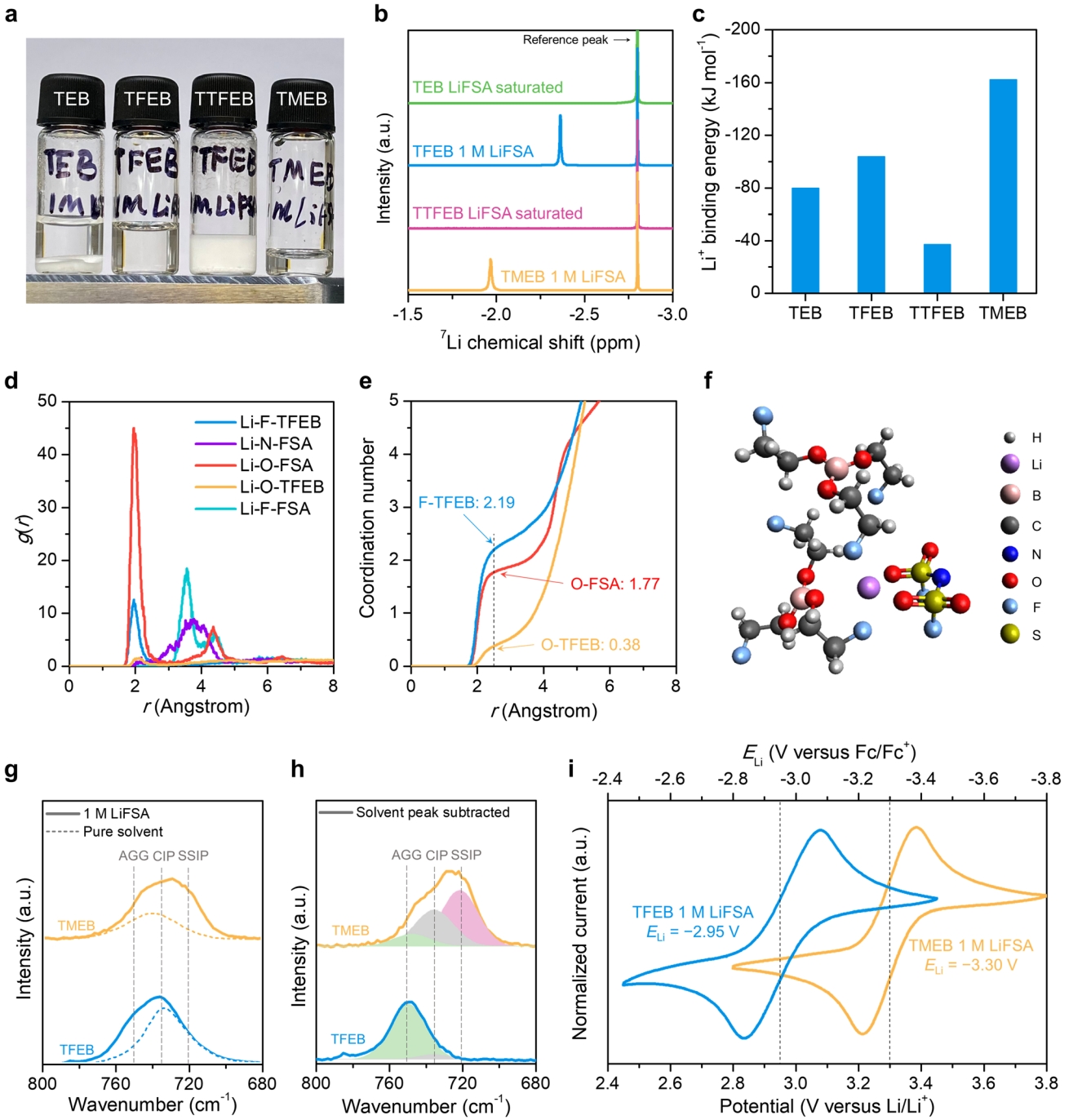

Fig. 2 Lithium salt solubility and ion solvation structure. (a) Digital photos of 1 M LiFSA salt in TEB, TFEB, TTFEB and TMEB. (b) ^{7}Li NMR spectra of LiFSA saturated TEB, 1 M LiFSA in TFEB, LiFSA saturated TTFEB and 1 M LiFSA in TMEB. (c) Binding energy between Li^{+} and borate ester solvents simulated by density functional theory (DFT) calculations. (d–f) *Ab initio* molecular dynamics (AIMD) simulations of 1 M LiFSA in TFEB: (d) radial distribution function (RDF) between lithium ions and possible coordination sites; (e) coordination number of lithium ions as a function of radius; (f) snapshot of a representative lithium solvation environment extracted from production run. (g) Raman spectra of 1 M LiFSA in TMEB and 1 M LiFSA in TFEB with pure solvent spectra background (SSIP: solvent separated ion pair; CIP: contact ion pair; AGG: salt aggregates). (h) Fitting of the FSA Raman peak after subtracting solvent background. (i) Cyclic voltammetry of borate ester electrolytes containing 1 mM ferrocene (Fc) with platinum as the working electrode and lithium metal as the counter and reference electrode. The dashed line indicates halfway potential between Fc oxidation and reduction peaks.

Does an anion coordinate to borate esters?

In prior reports, it is generally believed that an anion can coordinate to the Lewis acidic boron atom in borate esters, which may promote salt dissociation and ion transport.[27–29] Therefore, we also investigated potential anion–solvent interactions using DFT and AIMD. As discussed in the ESI (Fig. S4†),

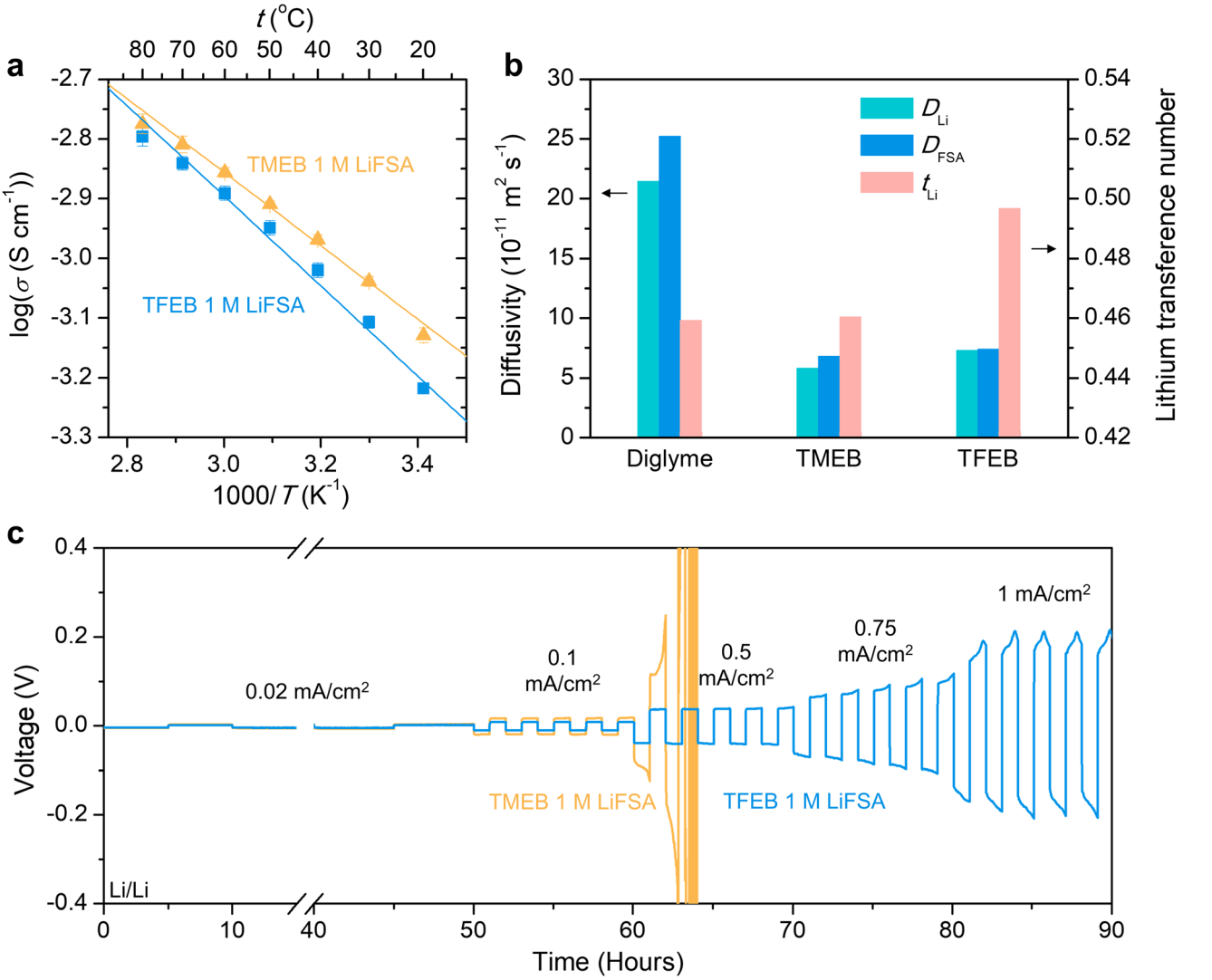

Fig. 3 Ion transport. (a) Ionic conductivity as a function of temperature of 1 M LiFSA in TMEB and 1 M LiFSA in TFEB. The lines are Arrhenius fitting of conductivity. (b) Ion diffusivities and lithium transference numbers of 1 M LiFSA in diglyme, 1 M LiFSA in TMEB and 1 M LiFSA in TFEB. (c) Critical current density test of 1 M LiFSA in TMEB and 1 M LiFSA in TFEB in lithium metal symmetrical cells (Li/Li). Voltage indicates overpotential *versus* Li/Li^+.

the simulation results do not show FSA coordination to the borate esters, which also agrees with the lithium transference number below 0.5 (Fig. 3b). While our preliminary study does not support anion–solvent coordination, future work will investigate other borate esters as well as probe anions with stronger coordination ability beyond FSA^-.

Ion transport

Ion transport in borate esters was probed by electrochemical impedance spectroscopy (EIS) and pulsed-field gradient nuclear magnetic resonance (PFG NMR) spectroscopy. Fig. 3a shows the ionic conductivity of 1 M LiFSA in borate ester solvents as a function of temperature. TFEB electrolyte shows slightly lower ionic conductivities than TMEB at all temperatures investigated, which is likely due to a lack of free ions as revealed previously by Raman spectra and cyclic voltammetry. Nonetheless, the ion pairing nature of TFEB electrolyte has positive effects on promoting the lithium transference number. Fig. 3b shows the ion diffusivity measured by PFG NMR and corresponding lithium transference number calculated as $t_{Li} = D_{Li}/(D_{Li} + D_{FSA})$. Since most Li^+ and FSA^- in TFEB are closely bound in ion pairs, they have almost identical diffusivity, which leads to a transference number close to 0.5. In contrast, TMEB electrolyte has a lower transference number similar to diglyme. In addition, 1 M LiFSA in TFEB electrolyte also has lower viscosity (7.85 mPa s) compared to 1 M LiFSA in TMEB electrolyte (11.19 mPa s) even though TFEB solvent has higher viscosity (5.12 mPa s) than TMEB solvent (2.84 mPa s) as shown in Table S1.† This indicates that TMEB has stronger interaction with LiFSA salt, which agrees with the solvation structure study.[37]

To study the effects of ion transport properties on battery cycling performance, critical current density tests were performed on lithium metal half cells (Li/Li cells). Fig. 3c shows that TFEB electrolyte maintains stable overpotentials at current

densities of 0.02, 0.1 and 0.5 mA cm^{-2} and can still be cycled at current density as high as 1 mA cm^{-2}. However, the overpotential of the TMEB cell increases rapidly at 0.5 mA cm^{-2} and the cell cannot be cycled at higher current densities. At 0.02 mA cm^{-2} and 0.1 mA cm^{-2} current densities where both electrolytes can be cycled, TFEB has lower overpotential compared to TMEB (9 mV *vs.* 18 mV at 0.1 mA cm^{-2}). As discussed later, the less resistive solid electrolyte interphase (SEI) formed in TFEB electrolyte as a result of ion pairing and solvent passivation outweighs the small difference in ionic conductivity and leads to the better rate capability of TFEB over TMEB.

Lithium metal compatibility

The influence of fluorination on lithium metal compatibility was investigated. Fig. 4a shows the Coulombic efficiency of lithium metal cycling measured by a modified Aurbach protocol at 0.1 mA cm^{-2}.[38] The fluorinated TFEB achieves a Coulombic efficiency of 97.1% that is much higher than that of non-fluorinated TMEB (51.7%). As shown in Fig. S5,† TFEB electrolyte maintains high Coulombic efficiency (97.1%) at 0.5 mA cm^{-2} current density while TMEB electrolyte can hardly cycle at higher current density. The good lithium metal compatibility of TFEB can also be probed by examining the lithium metal morphology using scanning electron microscopy (SEM). Fig. 4b shows that lithium metal deposited in TFEB electrolyte (0.5 mA cm^{-2} to 1.5 mA h cm^{-2} in the Li/Cu cell) has a desired chunky morphology with granular size in microns.[9] In contrast, TMEB electrolyte produces a more dendritic lithium morphology composed of lithium whiskers (Fig. 4c). To exclude the effect of rate capability, Fig. S6† shows the lithium metal morphology in TMEB electrolyte deposited at lower current density (0.1 mA cm^{-2} to 1.5 mA h cm^{-2} in the Li/Cu cell), where no significant improvement is observed compared to the morphology at 0.5 mA cm^{-2}. The stark contrast between TFEB and TMEB in lithium metal Coulombic efficiency and lithium morphology indicates that fluorination of borate esters significantly improves their performance with lithium metal.

To explain the superior lithium metal compatibility of TFEB, interfacial resistance in Li/Li cells was probed by EIS. As shown in Fig. S7,† TFEB leads to a much lower solid electrolyte interphase (SEI) resistance (14.44 Ω cm^2) than TMEB (110.14 Ω cm^2). The lower SEI resistance enables faster lithium ion diffusion through the SEI, which likely promotes continuous growth of lithium particles into larger size and improves lithium deposition/stripping reversibility.[39] X-ray photoelectron spectroscopy (XPS) was used to study the chemical composition of the lithium metal SEI. Three electrolytes: 1 M LiFSA in TFEB, 1 M LiFSA in TMEB and $LiClO_4$ saturated TFEB (<0.2 M) were studied to decouple the contribution of solvent and salt in the SEI. Fig. 4d and e show the C 1s and O 1s spectra of the lithium metal SEI, where common SEI components such as C=O, C–O, C–C/C–H and Li_2O are observed for all three electrolytes.[40] Interestingly, Fig. 4f shows that regardless of anion selection,

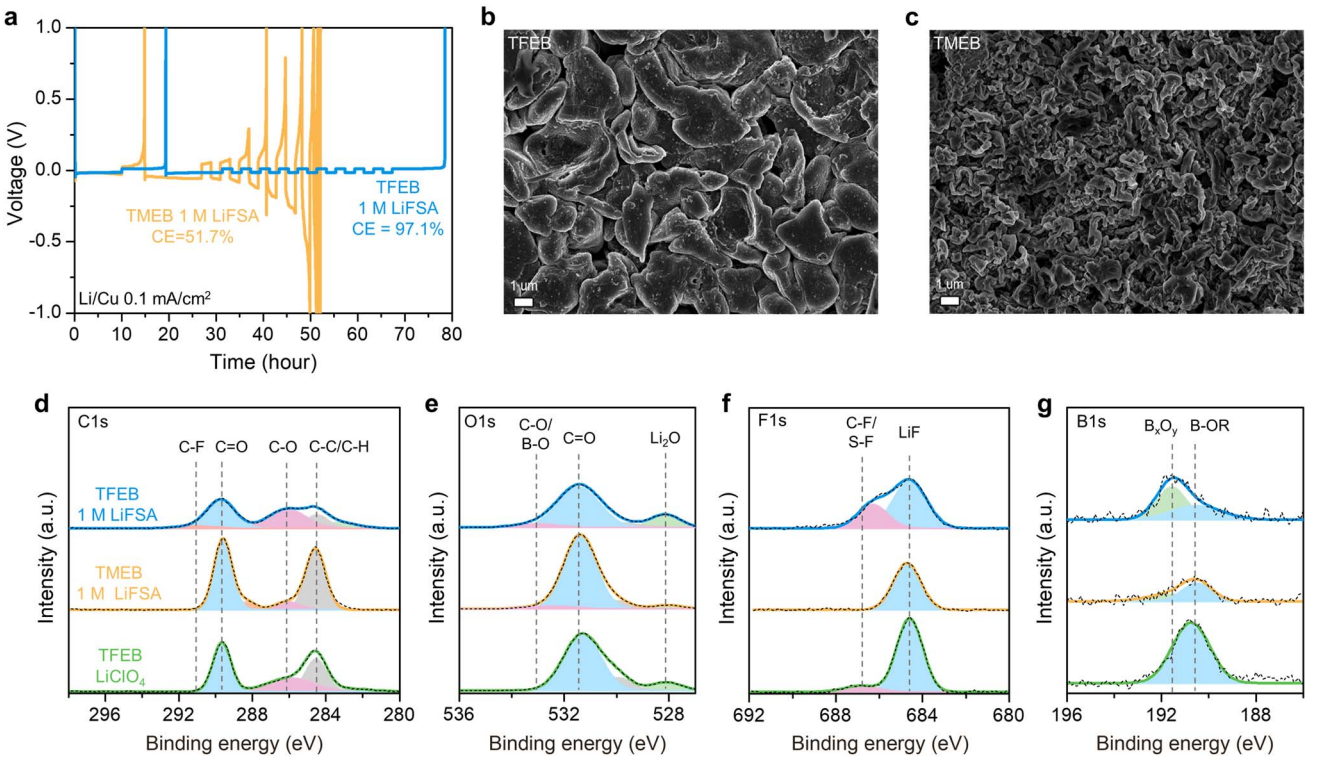

Fig. 4 Lithium metal compatibility. (a) Coulombic efficiency test in lithium metal/copper (Li/Cu) cells using a modified Aurbach protocol at 0.1 mA cm^{-2}. Voltage indicates overpotential *versus* Li/Li^+. (b and c) SEM images of lithium metal deposited in (b) 1 M LiFSA in TFEB and (c) 1 M LiFSA in TMEB. (d–g) XPS spectra of lithium metal deposited in 1 M LiFSA in TFEB, 1 M LiFSA in TMEB and $LiClO_4$ saturated TFEB (TFEB $LiClO_4$). Lithium metal was deposited at 0.5 mA cm^{-2} to 1.5 mA h cm^{-2} in Li/Cu cells for SEM and XPS.

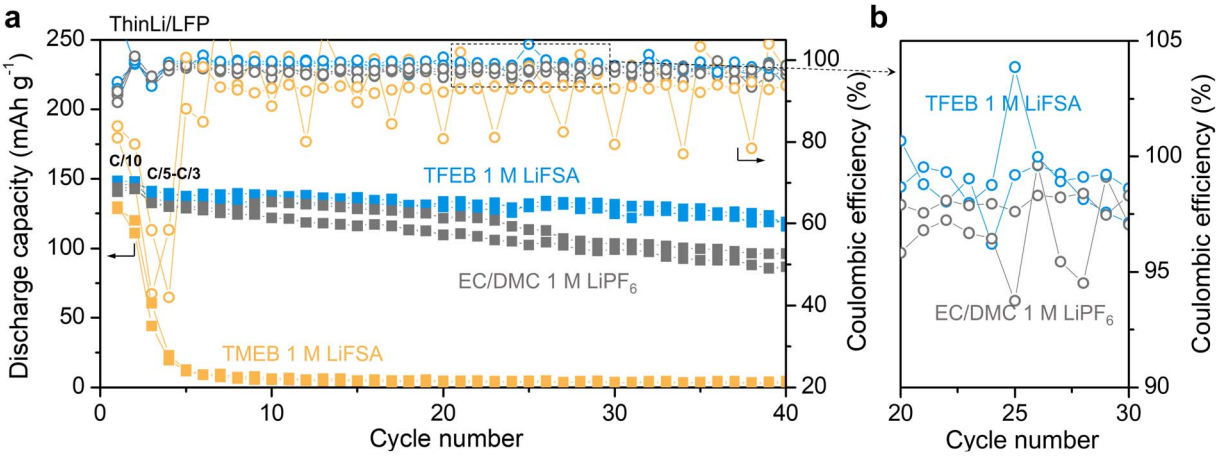

Fig. 5 Lithium metal cell cycling. (a) Galvanostatic cycling of 20 μm lithium metal/$LiFePO_4$ (ThinLi/LFP) cells. Two replicates of each electrolyte are shown. (b) Enlarged view of Coulombic efficiency of TFEB and EC/DMC cells at a later stage of cycling.

TFEB electrolytes produce significant amount of LiF. As is widely acknowledged in the literature, a high LiF concentration may improve SEI robustness, which may lead to the improved lithium compatibility of TFEB electrolyte.[41] Additionally, the fact that TFEB $LiClO_4$ electrolyte also produces a high concentration of LiF proves that a significant fraction of LiF originates from TFEB solvent molecules. As shown in Fig. 4g, B 1s spectra also support that borate ester solvents contribute to the SEI since B_xO_y and B–OR components are observed in all three electrolytes. To speculate regarding the borate ester degradation pathway, DFT calculations were performed on the reduction of borate esters. As shown in Fig. S8,† the TMEB molecule prefers a reduction pathway *via* breaking the B–O–C bond while TFEB has a more favored (higher reduction potential) reduction pathway by breaking the C–F bond and eliminating a fluoride. DFT calculations support XPS observations that TFEB solvent degradation likely makes a significant contribution to the SEI.

Full cell cycling

To illustrate that fluorinated borate ester electrolytes can be viable candidates for lithium metal batteries, cycling of lithium metal (20 μm thickness)/$LiFePO_4$ (ThinLi/LFP, n/p ≈ 3.2, 1C ≈ 1.81 mA cm^{-2}, and E/C ≈ 26 g Ah^{-1}) full cells with limited lithium content was performed. Fig. 5a shows that TFEB electrolyte can enable stable cycling of ThinLi/LFP cells while the TMEB electrolyte leads to rapid capacity decay from the third cycle. In addition, TFEB electrolyte outperforms EC/DMC 1 M $LiPF_6$ electrolyte with better capacity retention at the 40th cycle (82% *vs.* 68%) and overall higher coulombic efficiency (Fig. 5b). Fig. S9† shows the voltage profile of ThinLi/LFP cells at selected cycles, where TFEB electrolyte maintains a stable voltage profile despite slow capacity decay and little polarization. To verify that the poor cycling performance of TMEB is not due to rate capability, lithium metal (375 μm thickness)/$LiFePO_4$ (Li/LFP) cells were cycled at varying current rates with five cycles at each rate. As Fig. S10† shows, the TMEB cell cannot be cycled even at C/10. By contrast, TFEB electrolyte can support cycling up to C/2 and full capacity can be recovered after cycling at 1C. The lithium metal full cell cycling results verify that the fluorination of borate ester greatly improves its ion solvation ability while also enabling stability against lithium metal.

Conclusions

This work studies the effect of fluorination degree on solvation ability of borate esters and proves that partially fluorinated groups can enable salt dissolution up to 1 M with fluorine as the main binding site. We synthesized a novel partially fluorinated borate ester TFEB and found that TFEB has surprisingly higher lithium salt solubility compared to its nonfluorinated TEB and heavily fluorinated TTFEB counterparts. Through DFT and AIMD simulations, we discovered that the $-CH_2F$ group in TFEB acts as the primary coordination site that leads to high lithium salt solubility. Owing to the ion solvation structure rich in ion pairing, TFEB electrolyte shows a high lithium transference number and facile lithium-ion transport despite moderate ionic conductivity. The high lithium metal Coulombic efficiency and stable Li/LFP full cell cycling support TFEB as a promising electrolyte solvent candidate for lithium metal batteries. While TFEB is only one example that still requires further optimization, we believe that the coordination ability of partially fluorinated groups highlighted in this work would broaden the scope of molecular design and enable novel fluorinated electrolytes for next generation batteries.

Experimental section

Materials

Boric anhydride (98%), 1,2-dimethoxyethane (anhydrous), diethylene glycol dimethyl ether (anhydrous), tris(2,2,2-trifluoroethyl) borate (97%), α,α,α-trifluorotoluene (anhydrous), *p*-toluenesulfonic acid monohydrate (99%) and 4 Å molecular sieves were purchased from Sigma-Aldrich. Toluene (certified ACS grade), 2-methoxyethanol (anhydrous) and 2-fluoroethanol (95%) were purchased from Fisher. Triethyl borate (97%) was purchased from TCI America. Lithium perchlorate

(99%) was purchased from Oakwood Chemical. Deuterated acetonitrile (≥99.8 atom % D) and deuterated dimethyl sulfoxide (≥99.8 atom % D) were purchased from Cambridge Isotope Laboratories. Lithium bis(fluorosulfonyl) amide (99%) was provided by Arkema Inc. All solvents used for preparing electrolytes were dried using 4 Å molecular sieves overnight inside an argon-filled glovebox (VigorTech, O_2 and H_2O < 1 ppm). Lithium salts were vacuum dried at 120 °C overnight in a heated glovebox antechamber before use and were not exposed to air at any time. Other chemicals were used as received.

A Celgard 2325 separator was purchased from Celgard LLC. The separator was cut into 18 mm diameter disks, washed multiple times using acetone and vacuum dried at 70 °C overnight before it was transferred into the argon glovebox without air exposure (using a BUCHI B-585 glass oven). All stainless steel coin cell parts were obtained from Xiamen TOB New Energy Technology. Lithium foil (375 μm thick) was purchased from Sigma-Aldrich. Lithium foil was polished with a brush to remove the oxide layer and cut into 12 mm diameter disks before use. The $LiFePO_4$ (LFP) electrode was kindly provided by Cell Analysis, Modeling, and Prototyping (CAMP) facility of Argonne National Laboratory. The LFP electrode has a total mass loading of 13.40 mg cm^{-2} with 90 wt% of Johnson Matthey LFP, 5 wt% of Timcal C-45 and 5 wt% of Solvay 5130 PVDF binder. The LFP electrode was cut into 12 mm diameter disks and vacuum dried at 120 °C overnight in a heated glovebox antechamber before use.

Synthesis

In the example of TFEB, 4.18 g B_2O_3 (1 eq.), 200 mL toluene, 24.6 g 2-fluoroethanol (6.4 eq.) and 0.2 g *p*-toluenesulfonic acid monohydrate (0.018 eq.) were added into a round-bottom flask under nitrogen protection. The mixture was heated to reflux and water was removed using a Dean–Stark apparatus. The reaction was kept refluxing for 4 hours until no more water was generated. Toluene was removed under vacuum and the remaining was purified by fractional distillation under reduced pressure (boiling point of 60 °C at ∼5 mbar). To minimize hydrolysis of the product in air, the receiving flask was refilled with nitrogen at the end of distillation and sealed before being transferred into the glovebox. 10.0 g (42% yield) of the TFEB product was collected as a colorless liquid.

TMEB was synthesized by reacting B_2O_3 with 2-methoxyethanol following a similar procedure. The TMEB product was collected as a colorless liquid in 51% yield with a boiling point of 82 °C at ∼5 mbar. NMR spectra of TFEB and TMEB can be found in Fig. S11.†

Physical characterization

Nuclear magnetic resonance (NMR) spectroscopy. NMR spectroscopy was performed on either a Bruker Ascend 9.4 T/400 MHz (1D spectra) or a Bruker Ultrashield Plus 11.7 T/500 MHz (pulsed-field gradient NMR) instrument. All NMR samples were prepared and sealed inside an argon filled glovebox. The NMR sample for synthesis products was prepared by dissolving several milligrams of product into 0.5 mL molecular-sieve-dried deuterated dimethyl sulfoxide. For the characterization of electrolyte solutions, a capillary tube setup was used as described in ref. 11 and 42 The LiFSA saturated solutions (TEB and TTFEB) were first passed through a PTFE filter (0.45 μm) while the electrolyte solutions (TMEB and TFEB) were directly filled into a capillary tube (New Era Enterprises) and sealed using a PTFE cap. For 1D ^{7}Li and ^{19}F NMR, a reference solution having 0.1 M $LiClO_4$ and 0.1% volumetric fraction of α,α,α-trifluorotoluene in deuterated acetonitrile was used. The reference solution peak of ^{7}Li NMR spectra was calibrated to −2.80 ppm (ref. 43) and the reference peak of ^{19}F NMR spectra was calibrated to −62.5 ppm.[44] For PFG NMR, around 0.5 mL of deuterated acetonitrile was added to an NMR tube (Wilmad) and the capillary tube with sealed electrolyte was added subsequently. The NMR tube was capped and sealed with parafilm before being tested using a Bruker Ultrashield Plus 11.7 T/500 MHz instrument following programs described in our previous work.[12]

Viscosity measurement. Viscosity of borate ester solvents and electrolytes was measured using a microVISC viscometer (RheoSense). Inside an argon-filled glovebox, the sample was inserted into a pipette. Then, measurements were performed directly after taking it out of the glovebox.

Raman spectroscopy. A HORIBA LabRAM HR Evolution Confocal Raman Microscope was used for Raman spectroscopy. A 532 nm ULF laser was used as the light source. The sample was prepared by sealing electrolytes in glass chambers inside an argon filled glovebox. The glass chamber was assembled using glass slides (Chemglass Life Science) and silicone isolators purchased from Grace Bio-Labs.

Scanning electron microscopy (SEM) and X-ray photoelectron spectroscopy (XPS) of lithium metal. The lithium sample was prepared in Li/Cu cells. Five precycles were first performed prior to lithium deposition to clean the copper surface (at a current density of 0.02 mA cm^{-2} between 0 V and 1 V). Lithium was then deposited on the copper electrode at a current of 0.5 mA cm^{-2} or 0.1 mA cm^{-2} to a capacity of 1.5 mA h cm^{-2}. Li/Cu cells were opened in an argon filled glovebox. Copper foil with lithium deposited was rinsed with 1,2-dimethoxyethane twice to remove lithium salt and dried under vacuum before testing. A Carl Zeiss Merlin field emission scanning electron microscope was used for SEM characterization. XPS analysis was performed using a PHI 5000 VersaProbe II System (Physical Electronics). The spectra were obtained using an Al Kα radiation ($h\nu$ = 1486.6 eV) beam (100 μm, 25 W), Ar^+ and electron beam sample neutralization, in fixed analyzer transmission mode. XPS spectra were aligned to the C–C component in the C 1s spectra at 284.6 eV.

Electrochemical characterization

Lithium potential test in Li/Pt cells. 200 μL electrolyte containing 1 mM ferrocene was added into a micro beaker cell with a platinum wire as the working electrode and a lithium wire as the counter and reference electrode. Cyclic voltammetry was performed at a scan rate of 5 mV s^{-1} for three scans (oxidation first) and the second scan was used for plotting and calculating lithium potential.

Coin cell preparation. All the electrochemical characterization studies except for the lithium potential test were performed in CR2032 type coin cells with the following configuration: negative case‖spring‖spacer‖anode (counter electrode)‖25 μL electrolyte‖1 separator‖25 μL electrolyte‖cathode (working electrode)‖spacer‖positive case.

Electrochemical impedance spectroscopy (EIS). Stainless steel/stainless steel (SS/SS) coin cells were tested inside an ESPEC environmental chamber (BTZ-133). Temperature was first set to 80 °C and cooled in 10 °C intervals to 20 °C while holding at each temperature for 1 hour before EIS measurement. A Biologic VSP-300 potentiostat was used to measure impedance spectra between 7 MHz and 100 Hz. To calculate realistic conductivity, raw conductivity was multiplied by a cell constant of 12.6, which is calibrated using 1 M LiFSA in TFEB electrolyte using a platinum-cell conductivity probe (Vernier).[12]

Coin cell cycling. A Neware BTS4000 battery tester was used to cycle Li/Li, Li/Cu and Li/LFP coin cells at 20 °C (±0.1 °C) or uncontrolled room temperature (~26 °C). All cells were rested for 10 hours before testing. Li/Li cells were first cycled from 0.02 mA cm^{-2} to 0.1 mA h cm^{-2} for five formation cycles and then cycled at current densities increasing from 0.1 mA cm^{-2} to 1 mA h cm^{-2} with a 1-hour duration of charge and discharge. For coulombic efficiency (CE) measurement in Li/Cu cells, a formation cycle was first performed by depositing lithium on the copper electrode for 10 hours and then stripping to 1 V. Afterward, a ten-hour deposition was performed followed by 10 cycles of two-hour deposition and two-hour stripping (yielding 0.2 mA h cm^{-2} for 0.1 mA cm^{-2}). Finally, lithium was stripped from the copper electrode until cell voltage reached 1 V. CE was calculated as the ratio of total stripping capacity over total depositing capacity (excluding the formation cycle). LFP cells were cycled in a voltage window of 2.9–3.8 V with current rates calculated based on the exact mass of the cathode material, using 150 mA h g^{-1} as the full capacity of LFP. For an average mass loading of 12.1 mg LFP per cm^2, 1C ≈ 1.81 mA cm^{-2}. For Cycling of ThinLi/LFP cells, two formation cycles at C/10 were first performed and then the cell was cycled at a C/5 charging rate and C/3 discharging rate. For the rate capability test of Li/LFP cells, five cycles were performed at each current rate.

Simulations

***Ab initio* molecular dynamics (AIMD) simulations.** The AIMD calculations were performed using CP2K (version 9.1).[45] The simulation box for pristine TFEB of size 20 × 20 × 20 $Å^3$ containing 29 TFEB molecules was first created by using Packmol.[46] This simulation box underwent constant pressure NPT ensemble calculations (at 300 K) for 5 ps to obtain the correct box size. Five molecules of LiFSA were then added to this box using Packmol. The initial 1 M LiFSA in the TFEB simulation box was annealed at 500 K for 5 ps (NVT ensemble) and then the final production run (NVT ensemble) was performed at 300 K for 15 ps. The RDF was calculated for trajectories from the final 13 ps production run using the MDAnalysis python library.[47] All AIMD calculations employed a double ζ basis set, GTH pseudopotentials using a 400 Ry cutoff for the auxiliary plane wave basis, the PBE functional along with Grimme's D3 dispersion correction, and periodic boundary conditions. The Nosé–Hoover thermostat was used for equilibration.[48]

Density functional theory (DFT) calculations. DFT calculations were performed using the Gaussian 16 computational package.[49] All geometries were optimized at the B3LYP/6-31G(d,p) level of theory. After stationary points were verified by the absence of imaginary frequencies, single point energies of the optimized geometries were calculated using B3LYP/6-311++G(d,p). Solvent effects were accounted for by employing the SMD model.[50] THF was selected because of its moderate dielectric constant. The Grimme's DFT-D3 method with BJ-damping (GD3BJ) was used for dispersion correction.[51] To calculate the binding energy, Gibbs free energies of solvents and solvent–ion clusters were calculated. Ion (lithium ion or anion) binding energy is defined as G(solvent + ion) − G(solvent) − G(ion). The reduction energy was calculated from G(solvent) − G(solvent$^-$), where the geometry of solvent$^-$ is optimized. The reduction energy value was divided by Faraday's constant and then 1.4 V was subtracted from it to convert to reduction potentials *versus* the Li/Li^+ electrode.[52]

Author contributions

C.·V. A. and Peiyuan Ma conceived the idea and designed the experiments. Peiyuan Ma performed most of the experiments and DFT calculations. R. K. performed AIMD simulation. M. C. V. collected the XPS data. K. H. W. collected part of the cycling data. Priyadarshini Mirmira contributed to data analysis. All authors contributed to the discussion. Peiyuan Ma and C.·V. A. wrote the manuscript, and all the authors contributed to editing the manuscript.

Conflicts of interest

A provisional patent containing molecular structures shown in this work has been filed.

Acknowledgements

This work was supported by the National Science Foundation (NSF) CAREER Award (CBET-2144454). This work made use of the shared facilities (Raman, SEM) at the University of Chicago Materials Research Science and Engineering Center, supported by the National Science Foundation under award number DMR-2011854. R. K. acknowledges support from the Eric and Wendy Schmidt AI in Science Postdoctoral Fellowship, a Schmidt Futures Program. Parts of this work (DSC, FTIR) were carried out at the Soft Matter Characterization Facility of the University of Chicago. NMR measurements were performed at the UChicago Chemistry NMR Facility. The DFT and AIMD simulations were performed with resources provided by the University of Chicago's Research Computing Center (RCC) and Argonne Leadership Computing Facility (ALCF) at Argonne National Laboratory. The authors thank Steve Trask and Andrew Jansen at Argonne's Cell Analysis, Modeling, and Prototyping (CAMP) facility for providing the LFP electrode. The authors thank

Edward F. Barry at Argonne National Laboratory for providing the 20 μm Li electrode.

References

1 D. Lin, Y. Liu and Y. Cui, Reviving the Lithium Metal Anode for High-Energy Batteries, *Nat. Nanotechnol.*, 2017, **12**(3), 194–206, DOI: 10.1038/nnano.2017.16.

2 F. Ding, W. Xu, X. Chen, J. Zhang, M. H. Engelhard, Y. Zhang, B. R. Johnson, J. V. Crum, T. A. Blake, X. Liu and J.-G. Zhang, Effects of Carbonate Solvents and Lithium Salts on Morphology and Coulombic Efficiency of Lithium Electrode, *J. Electrochem. Soc.*, 2013, **160**(10), A1894–A1901, DOI: 10.1149/2.100310jes.

3 S. Chen, J. Zheng, D. Mei, K. S. Han, M. H. Engelhard, W. Zhao, W. Xu, J. Liu and J.-G. Zhang, High-Voltage Lithium-Metal Batteries Enabled by Localized High-Concentration Electrolytes, *Adv. Mater.*, 2018, **30**(21), 1706102, DOI: 10.1002/adma.201706102.

4 C. V. Amanchukwu, The Electrolyte Frontier: A Manifesto, *Joule*, 2020, **4**(2), 281–285, DOI: 10.1016/j.joule.2019.12.009.

5 S. Jiao, X. Ren, R. Cao, M. H. Engelhard, Y. Liu, D. Hu, D. Mei, J. Zheng, W. Zhao, Q. Li, N. Liu, B. D. Adams, C. Ma, J. Liu, J.-G. Zhang and W. Xu, Stable Cycling of High-Voltage Lithium Metal Batteries in Ether Electrolytes, *Nat. Energy*, 2018, **3**, 739–746, DOI: 10.1038/s41560-018-0199-8.

6 Y. Yamada and A. Yamada, Review—Superconcentrated Electrolytes for Lithium Batteries, *J. Electrochem. Soc.*, 2015, **162**(14), A2406–A2423, DOI: 10.1149/2.0041514jes.

7 Y. Yamada, K. Furukawa, K. Sodeyama, K. Kikuchi, M. Yaegashi, Y. Tateyama and A. Yamada, Unusual Stability of Acetonitrile-Based Superconcentrated Electrolytes for Fast-Charging Lithium-Ion Batteries, *J. Am. Chem. Soc.*, 2014, **136**(13), 5039–5046, DOI: 10.1021/ja412807w.

8 X. Cao, H. Jia, W. Xu and J.-G. Zhang, Review—Localized High-Concentration Electrolytes for Lithium Batteries, *J. Electrochem. Soc.*, 2021, **168**(1), 010522, DOI: 10.1149/1945-7111/abd60e.

9 J. Qian, W. A. Henderson, W. Xu, P. Bhattacharya, M. Engelhard, O. Borodin and J.-G. Zhang, High Rate and Stable Cycling of Lithium Metal Anode, *Nat. Commun.*, 2015, **6**(1), 6362, DOI: 10.1038/ncomms7362.

10 X. Cao, X. Ren, L. Zou, M. H. Engelhard, W. Huang, H. Wang, B. E. Matthews, H. Lee, C. Niu, B. W. Arey, Y. Cui, C. Wang, J. Xiao, J. Liu, W. Xu and J.-G. Zhang, Monolithic Solid–Electrolyte Interphases Formed in Fluorinated Orthoformate-Based Electrolytes Minimize Li Depletion and Pulverization, *Nat. Energy*, 2019, **4**(9), 796–805, DOI: 10.1038/s41560-019-0464-5.

11 C. V. Amanchukwu, Z. Yu, X. Kong, J. Qin, Y. Cui and Z. Bao, A New Class of Ionically Conducting Fluorinated Ether Electrolytes with High Electrochemical Stability, *J. Am. Chem. Soc.*, 2020, **142**(16), 7393–7403, DOI: 10.1021/jacs.9b11056.

12 P. Ma, P. Mirmira and C. V. Amanchukwu, Effect of Building Block Connectivity and Ion Solvation on Electrochemical Stability and Ionic Conductivity in Novel Fluoroether Electrolytes, *ACS Cent. Sci.*, 2021, **7**(7), 1232–1244, DOI: 10.1021/acscentsci.1c00503.

13 Z. Yu, H. Wang, X. Kong, W. Huang, Y. Tsao, D. G. Mackanic, K. Wang, X. Wang, W. Huang, S. Choudhury, Y. Zheng, C. V. Amanchukwu, S. T. Hung, Y. Ma, E. G. Lomeli, J. Qin, Y. Cui and Z. Bao, Molecular Design for Electrolyte Solvents Enabling Energy-Dense and Long-Cycling Lithium Metal Batteries, *Nat. Energy*, 2020, **5**(7), 526–533, DOI: 10.1038/s41560-020-0634-5.

14 Z. Yu, P. E. Rudnicki, Z. Zhang, Z. Huang, H. Celik, S. T. Oyakhire, Y. Chen, X. Kong, S. C. Kim, X. Xiao, H. Wang, Y. Zheng, G. A. Kamat, M. S. Kim, S. F. Bent, J. Qin, Y. Cui and Z. Bao, Rational Solvent Molecule Tuning for High-Performance Lithium Metal Battery Electrolytes, *Nat. Energy*, 2022, **7**(1), 94–106, DOI: 10.1038/s41560-021-00962-y.

15 W. Xue, Z. Shi, M. Huang, S. Feng, C. Wang, F. Wang, J. Lopez, B. Qiao, G. Xu, W. Zhang, Y. Dong, R. Gao, Y. Shao-Horn, J. A. Johnson and J. Li, FSI-Inspired Solvent and "Full Fluorosulfonyl" Electrolyte for 4 V Class Lithium-Metal Batteries, *Energy Environ. Sci.*, 2020, **13**(1), 212–220, DOI: 10.1039/C9EE02538C.

16 W. Xue, M. Huang, Y. Li, Y. Guang Zhu, R. Gao, X. Xiao, W. Zhang, S. Li, G. Xu, Y. Yu, P. Li, J. Lopez, D. Yu, Y. Dong, W. Fan, Z. Shi, R. Xiong, C.-J. Sun, I. Hwang, W.-K. Lee, Y. Shao-Horn, J. A. Johnson and J. Li, Ultra-High-Voltage Ni-Rich Layered Cathodes in Practical Li Metal Batteries Enabled by a Sulfonamide-Based Electrolyte, *Nat. Energy*, 2021, **6**, 495–505, DOI: 10.1038/s41560-021-00792-y.

17 T. Zhou, Y. Zhao, M. El Kazzi, J. W. Choi and A. Coskun, Integrated Ring-Chain Design of a New Fluorinated Ether Solvent for High-Voltage Lithium-Metal Batteries, *Angew. Chem., Int. Ed.*, 2022, e202115884, DOI: 10.1002/anie.202115884.

18 Y. Zhao, T. Zhou, T. Ashirov, M. E. Kazzi, C. Cancellieri, L. P. H. Jeurgens, J. W. Choi and A. Coskun, Fluorinated Ether Electrolyte with Controlled Solvation Structure for High Voltage Lithium Metal Batteries, *Nat. Commun.*, 2022, **13**(1), 2575, DOI: 10.1038/s41467-022-29199-3.

19 Y. Zhao, T. Zhou, M. Mensi, J. W. Choi and A. Coskun, Electrolyte Engineering via Ether Solvent Fluorination for Developing Stable Non-Aqueous Lithium Metal Batteries, *Nat. Commun.*, 2023, **14**(1), 299, DOI: 10.1038/s41467-023-35934-1.

20 Y. Zhao, T. Zhou, L. P. H. Jeurgens, X. Kong, J. W. Choi and A. Coskun, Electrolyte Engineering for Highly Inorganic Solid Electrolyte Interphase in High-Performance Lithium Metal Batteries, *Chem*, 2023, **9**(3), 682–697, DOI: 10.1016/j.chempr.2022.12.005.

21 S.-J. Park, J.-Y. Hwang, C. S. Yoon, H.-G. Jung and Y.-K. Sun, Stabilization of Lithium-Metal Batteries Based on the in Situ Formation of a Stable Solid Electrolyte Interphase Layer, *ACS*

Appl. Mater. Interfaces, 2018, **10**(21), 17985–17993, DOI: 10.1021/acsami.8b04592.

22 X. Fan, L. Chen, O. Borodin, X. Ji, J. Chen, S. Hou, T. Deng, J. Zheng, C. Yang, S.-C. Liou, K. Amine, K. Xu and C. Wang, Non-Flammable Electrolyte Enables Li-Metal Batteries with Aggressive Cathode Chemistries, *Nat. Nanotechnol.*, 2018, **13**(8), 715–722, DOI: 10.1038/s41565-018-0183-2.

23 K. M. Abraham, J. L. Goldman and D. L. Natwig, Characterization of Ether Electrolytes for Rechargeable Lithium Cells, *J. Electrochem. Soc.*, 1982, **129**(11), 2404–2409, DOI: 10.1149/1.2123556.

24 P. Ma, P. Mirmira, P. J. Eng, S.-B. Son, I. D. Bloom, A. S. Filatov and C. V. Amanchukwu, Co-Intercalation-Free Ether Electrolytes for Graphitic Anodes in Lithium-Ion Batteries, *Energy Environ. Sci.*, 2022, **15**(11), 4823–4835, DOI: 10.1039/D2EE01489K.

25 C. S. Rustomji, Y. Yang, T. K. Kim, J. Mac, Y. J. Kim, E. Caldwell, H. Chung and Y. S. Meng, Liquefied Gas Electrolytes for Electrochemical Energy Storage Devices, *Science*, 2017, **356**(6345), eaal4263, DOI: 10.1126/science.aal4263.

26 Z. Yu, W. Yu, Y. Chen, L. Mondonico, X. Xiao, Y. Zheng, F. Liu, S. T. Hung, Y. Cui and Z. Bao, Tuning Fluorination of Linear Carbonate for Lithium-Ion Batteries, *J. Electrochem. Soc.*, 2022, **169**(4), 40555, DOI: 10.1149/1945-7111/ac67f5.

27 M. A. Mehta and T. Fujinami, Li^+ Transference Number Enhancement in Polymer Electrolytes by Incorporation of Anion Trapping Boroxine Rings into the Polymer Host, *Chem. Lett.*, 1997, **26**(9), 915–916, DOI: 10.1246/cl.1997.915.

28 F. Zhou, D. R. MacFarlane and M. Forsyth, Boroxine Ring Compounds as Dissociation Enhancers in Gel Polyelectrolytes, *Electrochim. Acta*, 2003, **48**(12), 1749–1758, DOI: 10.1016/S0013-4686(03)00151-8.

29 H. S. Lee, The Synthesis of a New Family of Boron-Based Anion Receptors and the Study of Their Effect on Ion Pair Dissociation and Conductivity of Lithium Salts in Nonaqueous Solutions, *J. Electrochem. Soc.*, 1998, **145**(8), 2813, DOI: 10.1149/1.1838719.

30 Y. Ma, Z. Zhou, C. Li, L. Wang, Y. Wang, X. Cheng, P. Zuo, C. Du, H. Huo, Y. Gao and G. Yin, Enabling Reliable Lithium Metal Batteries by a Bifunctional Anionic Electrolyte Additive, *Energy Storage Mater.*, 2018, **11**, 197–204, DOI: 10.1016/j.ensm.2017.10.015.

31 L. Wang, Y. Ma, P. Wang, S. Lou, X. Cheng, P. Zuo, C. Du, Y. Gao and G. Yin, Interface Modifications by Tris(2,2,2-Trifluoroethyl) Borate for Improving the High-Voltage Performance of $LiNi_1/3Co_1/3Mn_1/3O_2$Cathode, *J. Electrochem. Soc.*, 2017, **164**(9), A1924–A1932, DOI: 10.1149/2.0891709jes.

32 F. Kaneko, Y. Masuda, M. Nakayama and M. Wakihara, Electrochemical Performances of Lithium Ion Battery Using Alkoxides of Group 13 as Electrolyte Solvent, *Electrochim. Acta*, 2007, **53**(2), 549–554, DOI: 10.1016/j.electacta.2007.07.005.

33 Y. Kato, K. Hasumi, S. Yokoyama, T. Yabe, H. Ikuta, Y. Uchimoto and M. Wakihara, Polymer Electrolyte Plasticized with PEG-Borate Ester Having High Ionic Conductivity and Thermal Stability, *Solid State Ionics*, 2002, **150**(3), 355–361, DOI: 10.1016/S0167-2738(02)00450-2.

34 S. H. Bauer and J. Y. Beach, The Structures of Methyl Borate and Trimethyl Triborine Trioxane. Interatomic Distances in Boron Compounds, *J. Am. Chem. Soc.*, 1941, **63**(5), 1394–1403, DOI: 10.1021/ja01850a075.

35 J. Wang, Y. Yamada, K. Sodeyama, C. H. Chiang, Y. Tateyama and A. Yamada, Superconcentrated Electrolytes for a High-Voltage Lithium-Ion Battery, *Nat. Commun.*, 2016, **7**(1), 12032, DOI: 10.1038/ncomms12032.

36 S. Ko, T. Obukata, T. Shimada, N. Takenaka, M. Nakayama, A. Yamada and Y. Yamada, Electrode Potential Influences the Reversibility of Lithium-Metal Anodes, *Nat. Energy*, 2022, **7**, 1217–1224, DOI: 10.1038/s41560-022-01144-0.

37 D. E. Goldsack and R. Franchetto, The Viscosity of Concentrated Electrolyte Solutions. I. Concentration Dependence at Fixed Temperature, *Can. J. Chem.*, 1977, **55**(6), 1062–1072, DOI: 10.1139/v77-148.

38 B. D. Adams, J. Zheng, X. Ren, W. Xu and J.-G. Zhang, Accurate Determination of Coulombic Efficiency for Lithium Metal Anodes and Lithium Metal Batteries, *Adv. Energy Mater.*, 2018, **8**(7), 1702097, DOI: 10.1002/aenm.201702097.

39 G. M. Hobold, K.-H. Kim and B. M. Gallant, Beneficial vs. Inhibiting Passivation by the Native Lithium Solid Electrolyte Interphase Revealed by Electrochemical Li^+ Exchange, *Energy Environ. Sci.*, 2023, **16**, 2247–2261, DOI: 10.1039/D2EE04203G.

40 X. Ren, L. Zou, X. Cao, M. H. Engelhard, W. Liu, S. D. Burton, H. Lee, C. Niu, B. E. Matthews, Z. Zhu, C. Wang, B. W. Arey, J. Xiao, J. Liu, J. G. Zhang and W. Xu, Enabling High-Voltage Lithium-Metal Batteries under Practical Conditions, *Joule*, 2019, **3**(7), 1662–1676, DOI: 10.1016/j.joule.2019.05.006.

41 J. Tan, J. Matz, P. Dong, J. Shen and M. Ye, A Growing Appreciation for the Role of LiF in the Solid Electrolyte Interphase, *Adv. Energy Mater.*, 2021, **11**(16), 2100046, DOI: 10.1002/aenm.202100046.

42 C. V. Amanchukwu, X. Kong, J. Qin, Y. Cui and Z. Bao, Nonpolar Alkanes Modify Lithium-Ion Solvation for Improved Lithium Deposition and Stripping, *Adv. Energy Mater.*, 2019, **9**(41), 1902116, DOI: 10.1002/aenm.201902116.

43 H. Günther, in *Lithium NMR*, eMagRes, 2007, DOI: 10.1002/9780470034590.emrstm0273.

44 C. Li, K. Suzuki, K. Yamaguchi and N. Mizuno, Phosphovanadomolybdic Acid Catalyzed Direct C–H Trifluoromethylation of (Hetero)Arenes Using $NaSO_2CF_3$ as the CF_3 Source and O_2 as the Terminal Oxidant, *New J. Chem.*, 2017, **41**(4), 1417–1420, DOI: 10.1039/C6NJ03654F.

45 T. D. Kühne, M. Iannuzzi, M. Del Ben, V. V. Rybkin, P. Seewald, F. Stein, T. Laino, R. Z. Khaliullin, O. Schütt, F. Schiffmann, D. Golze, J. Wilhelm, S. Chulkov, M. H. Bani-Hashemian, V. Weber, U. Borštnik, M. Taillefumier, A. S. Jakobovits, A. Lazzaro, H. Pabst, T. Müller, R. Schade, M. Guidon, S. Andermatt, N. Holmberg, G. K. Schenter, A. Hehn, A. Bussy, F. Belleflamme, G. Tabacchi, A. Glöß, M. Lass, I. Bethune,

C. J. Mundy, C. Plessl, M. Watkins, J. VandeVondele, M. Krack and J. Hutter, CP2K: An Electronic Structure and Molecular Dynamics Software Package – Quickstep: Efficient and Accurate Electronic Structure Calculations, *J. Chem. Phys.*, 2020, **152**(19), 194103, DOI: **10.1063/5.0007045**.

46 L. Martínez, R. Andrade, E. G. Birgin and J. M. Martínez, PACKMOL: A Package for Building Initial Configurations for Molecular Dynamics Simulations, *J. Comput. Chem.*, 2009, **30**(13), 2157–2164, DOI: **10.1002/jcc.21224**.

47 N. Michaud-Agrawal, E. J. Denning, T. B. Woolf and O. Beckstein, MDAnalysis: A Toolkit for the Analysis of Molecular Dynamics Simulations, *J. Comput. Chem.*, 2011, **32**(10), 2319–2327, DOI: **10.1002/jcc.21787**.

48 G. J. Martyna, M. L. Klein and M. Tuckerman, Nosé–Hoover Chains: The Canonical Ensemble via Continuous Dynamics, *J. Chem. Phys.*, 1992, **97**(4), 2635–2643, DOI: **10.1063/1.463940**.

49 M. J. Frisch, G. W. Trucks, H. B. Schlegel, G. E. Scuseria, M. A. Robb, J. R. Cheeseman, G. Scalmani, V. Barone, G. A. Petersson, H. Nakatsuji, X. Li, M. Caricato, A. V. Marenich, J. Bloino, B. G. Janesko, R. Gomperts, B. Mennucci, H. P. Hratchian, J. V. Ortiz, A. F. Izmaylov, J. L. Sonnenberg, D. Williams-Young, F. Ding, F. Lipparini, F. Egidi, J. Goings, B. Peng, A. Petrone, T. Henderson, D. Ranasinghe, V. G. Zakrzewski, J. Gao, N. Rega, G. Zheng, W. Liang, M. Hada, M. Ehara, K. Toyota, R. Fukuda, J. Hasegawa, M. Ishida, T. Nakajima, Y. Honda, O. Kitao, H. Nakai, T. Vreven, K. Throssell, J. A. Montgomery Jr, J. E. Peralta, F. Ogliaro, M. J. Bearpark, J. J. Heyd, E. N. Brothers, K. N. Kudin, V. N. Staroverov, T. A. Keith, R. Kobayashi, J. Normand, K. Raghavachari, A. P. Rendell, J. C. Burant, S. S. Iyengar, J. Tomasi, M. Cossi, J. M. Millam, M. Klene, C. Adamo, R. Cammi, J. W. Ochterski, R. L. Martin, K. Morokuma, O. Farkas, J. B. Foresman and D. J. Fox, *Gaussian 16 Rev*. A.03, Wallingford, CT, 2016.

50 A. V. Marenich, C. J. Cramer and D. G. Truhlar, Universal Solvation Model Based on Solute Electron Density and on a Continuum Model of the Solvent Defined by the Bulk Dielectric Constant and Atomic Surface Tensions, *J. Phys. Chem. B*, 2009, **113**(18), 6378–6396, DOI: **10.1021/jp810292n**.

51 S. Grimme, S. Ehrlich and L. Goerigk, Effect of the Damping Function in Dispersion Corrected Density Functional Theory, *J. Comput. Chem.*, 2011, **32**(7), 1456–1465, DOI: **10.1002/jcc.21759**.

52 O. Borodin, W. Behl and T. R. Jow, Oxidative Stability and Initial Decomposition Reactions of Carbonate, Sulfone, and Alkyl Phosphate-Based Electrolytes, *J. Phys. Chem. C*, 2013, **117**(17), 8661–8682, DOI: **10.1021/jp400527c**.